Application of Compressive Sensing for Gravitational Microlensing Events

Asmita Korde-Patel[a,b,*], **Richard K. Barry**[a], **Tinoosh Mohsenin**[b]
[a]NASA Goddard Space Flight Center, Greenbelt, MD, USA
[b]University of Maryland, Baltimore County, Baltimore, MD, USA

Abstract. Compressive sensing is a novel mathematical technique for simultaneous data acquisition and compression. This technique is particularly apt for time-series photometric measurements. In this work we apply compressive sensing to time-series photometric measurements specifically obtained due to gravitational microlensing events. We show through simulation modelling the error sensitivity for detecting microlensing event parameters. Particularly, we show the relation of the amount of error and its impact on the microlensing parameters of interest. We derive statistical error bounds to apply those as a baseline for analyzing the effectiveness of compressive sensing application. Our results conclude that for single and binary microlensing events we can obtain error less than 1% over a 3-pixel radius of the center of the microlensing star by using 25% Nyquist rate measurements.

Keywords: Compressive Sensing, Gravitational Microlensing, Data Acquisition and Compression.

*Asmita Korde-Patel, asmita.a.korde@nasa.gov

1 Introduction

Compressive sensing (CS) is a simultaneous data acquisition and compression technique, where data compression is performed at the detector front-end itself. CS is a mathematical theory which allows sampling at sub-Nyquist rate by exploiting sparsity in data sets. In this work, we assess the application of CS to gravitational microlensing events. Our work is primarily applicable for space-flight instruments, which exhibit tremendous limitations for on-board space flight resources as well as data transmission bandwidth.

Gravitational microlensing is an astronomical phenomena during which a massive body, such as a star or a black hole, or a system of bodies, may pass in front of a distant source star causing the deflection of light from the source, effectively briefly magnifying and brightening that source. Using this technique exoplanets can be detected. The phenomenology of microlensing requires the exceedingly precise alignment of a source star and an intervening massive body. Consequently, microlensing events are very rare – thus sparse in both time and space. These, hence, form an excellent evaluation platform for the development and application of CS. The mathematical technique implemented for CS exploits this sparsity inherent in gravitational microlensing and encodes the image during acquisition, significantly reducing data volume and for space flight instruments- reduces on-board resources.[1,2] Similar to traditional methods, we apply data acquisition of the spatial images, followed by differencing to obtain a light curve representing a microlensing star over time. The differencing provides the relative change in pixel magnitude over time, as shown in Figure 1.

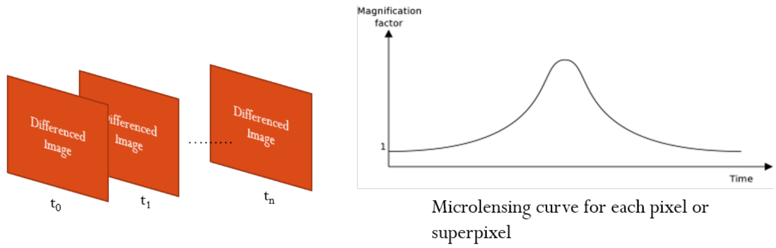

Fig 1: Image differencing to generate a light curve over time, representing the change in magnification of a microlensing star

Figure 2 shows the placement of a CS detector in a high level block diagram.

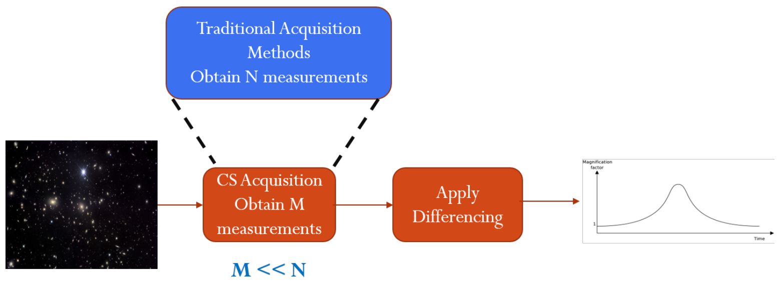

Fig 2: CS detector will replace a traditional detector to acquire spatial images. The data acquired from the detector will be used to generate photometric light curves for microlensing events

In our previous work, we did preliminary analysis on the effects of CS on transient photometric measurements. In this work, we specifically analyze single and binary microlensing events and the implications of CS reconstruction on gravitational microlensing parameters of interest.

1.1 Compressive Sensing

Compressive sensing is a mathematical theory for sampling at a rate much lower than the Nyquist rate, and yet, reconstructing the signal back with little or no loss of information. The signal is reconstructed by solving an underdetermined system. Sparsity in data sets is a key component required for the accuracy in reconstruction using CS methods. If it is not sparse in the sampling domain, we can transform it to a sparse domain, perform the reconstruction and then transform it back to the original domain.[3,4] In a CS architecture, to acquire a signal of size n, we collect m measurements, where $m << n$. One measurement sample consists of a collective sum. We solve for equation (1) to determine x through the observation y.[5–8]

$$y_{m\mathrm{x}1} = A_{m\mathrm{x}n} x_{n\mathrm{x}1} \tag{1}$$

Using the acquired measurements vector y and the known measurement matrix A, we can solve for a sparse x by applying various techniques, including greedy algorithms and optimization algorithms. Various reconstruction algorithms are discussed in the work by Pope.[9]

1.2 Gravitational Micorlensed Events

In gravitational lensing, the surface brightness, which is the flux per area, is conserved. The total flux increases or decreases, since the area increases or decreases. In microlensing, distinct images, due to the gravitational effects of the lensing system, are not seen, but rather, magnification or demagnification of the source star is observed; the images are not resolved. Since the Jacobian matrix gives the amount of change in the source star flux in each direction, the transformation of the original source to the "stretched" source, can be mapped by the Jacobian. The absolute value of the inverse of determinant gives the amount of magnification.

Einstein's ring forms when there is an exact alignment of the source, lens and observer and is an important parameter for the basis of gravitational microlensing equations. Einstein's ring radius, θ_E can be defined by equation 2.

$$\theta_E = \sqrt{\frac{4GMD_{LS}}{c^2 D_L D_S}} \tag{2}$$

where M is the the mass of the lensing system, D_{LS} is the distance from the lens to the source, D_L is the distance from the observer to the lensing system, and D_S is the distance from the observer to the source.[10,11]

1.3 Single Lens Gravitationally Microlensed events

Here we describe the amplification value for each time as the source star moves in relation to the lensing system. Let $\mathbf{u}$ represent source position, and $\mathbf{y}$ represent image position, normalized by θ_E. Then, the lensing equation for a single lens microlensing event can be given as equation 3.[10]

$$y_{\pm} = \pm \frac{\sqrt{u^2 + 4} \pm u}{2} \tag{3}$$

Total amplification of the two images formed is given by

$$A(u) = \frac{u^2 + 2}{u\sqrt{u^2 + 4}} \tag{4}$$

Due to the relative motion between the lens and source, amplification is dependent on the position of the source image at each time, t. Equation 5 shows the position of the source at each time given the trajectory the source takes.[10]

$$u(t) = \left[u_0^2 + \left(\frac{t - t_0}{t_E} \right)^2 \right]^{1/2} \tag{5}$$

The trajectory is defined by the impact parameter, u_0, which is the minimum apparent separation between the lens and source in units of θ_E. Einstein ring radius crossing time is given by t_E and the time of peak magnification is given by t_0.[10] The amplification with time dependency is shown in equation 6

$$A(t) = \frac{u_0^2 + \left(\frac{t - t_0}{t_E}\right)^2 + 2}{\left[u_0^2 + \left(\frac{t - t_0{}^2}{t_E}\right)\right]^{1/2} \left[u_0^2 + \left(\frac{t - t_0}{t_E}\right)^2 + 4)\right]^{1/2}} \tag{6}$$

1.3.1 Error sensitivity

In this section, we show the relation of error to the sensitivity of the parameter θ_E. For an error of $\epsilon(t)$ in the change in amplification at any given time, the amplification at each time changes by $A(t) + \epsilon(t)$. This change in $\epsilon(t)$ at each time, t, changes the amplification equation derived due to two images resulting from a single lens microlensing event. Using equation 5, equation 6 can be written as 7.

$$A(t) = \frac{u^2(t) + 2}{u(t)\sqrt{[u^2(t) + 4]}} \tag{7}$$

Incorporating error, we get equation 8.

$$A(t) + \epsilon(t) = \frac{u^2(t) + 2 + \epsilon(t)[u(t)\sqrt{u^2(t) + 4}]}{u(t)\sqrt{u^2(t) + 4}} \tag{8}$$

From equation 8, it is evident that a change in the light curve due to an error, $\epsilon(t)$, will not merely result in a change in u_0, but rather a change in the lensing system itself. That is, the light curve produced would not be accurately mapped to a lensing system.

In order to better understand analytical effects of error on science parameters, here, we show the effect of the change in science parameter and its implication on the amplification value. For a change of γ in the value of θ_E, which depends on the properities of the lensing system, as noted in equation 2, we can define, $\tilde{\theta_E}$ as

$$\tilde{\theta}_E = \gamma\theta_E \tag{9}$$

Using this $\tilde{\theta_E}$ in the lensing system, we derive the new amplification curve shown in equation 11. In our model, for $\tilde{A(t)}$, we scale u_0 by θ_E and not by $\tilde{\theta}_E$ to keep the same u_0 scale for comparison to $A(t)$.

$$A(u) = \frac{u^2 + 2\gamma^2}{u\sqrt{u^2 + 4\gamma^2}} \tag{10}$$

Expanding to include the definition of $u(t)$, we get equation 11.

$$\tilde{A}(t) = \frac{u_0^2 + \left(\frac{t - t_0}{t_E}\right)^2 + 2\gamma^2}{\left[u_0^2 + \left(\frac{t - t_0}{t_E}\right)^2\right]^{1/2} \left[u_0^2 + \left(\frac{t - t_0}{t_E}\right)^2 + 4\gamma^2)\right]^{1/2}} \tag{11}$$

To analyze the effect of compressive sensing errors, for single microlensing events, we consider the effect of θ_E on the amplification value. In equation 6, u_0 is in units of θ_E. Hence, a change of γ in θ_E, will directly affect the mass and distance parameters, M, D_LS, D_L and D_S of the lensing system. Our CS based modelling incorporates γ to determine the effect of errors due to CS application on the value of θ_E.

For astronomical measurements, the detector measures the flux of the source star. Hence, for microlensing, total flux received from the source star is given by equation 12.

$$F(t) = F_s A(t) + F_b \tag{12}$$

where F_s is the flux from the source, A is the amplification amount and F_b is the blended flux. In our simulation modelling, we use F_b = 0 for simplicity.

1.4 Binary Lensed Gravitational Microlensed Events

A binary microlensed system consists of two lensing bodies, which act as a lens, deflecting the light from the observed source star. Here, we have two lensing bodies with mass, m_1 and m_2, where $m_1 + m_2 = M$. The source position is given by $\bar{\Psi}$. The image positions are given by equation 13.[10]

$$\bar{z} = \bar{\Psi} + \frac{m_1}{z - z_1} + \frac{m_2}{z - z_2} \tag{13}$$

The amplification due to this lensing system is given by the ratio of the total area of the images to the total area of the source. Finding the amplification at each time is given by the following process:[12]

1. Find the roots of the polynomial given by the lensing equation 13.
2. Determine the boundaries of the images given the critical curves. The Jacobian of the lensing equation is used to determine the boundaries.
3. Find the area of all the images bounded by the critical curves.
4. Total amplification is given by equation 14.

$$A = \frac{A_I}{A_S} \tag{14}$$

where A is the amplification value, A_I is the total area of all the images produced due the lensing, and A_S is the area of source star.

For an error, ϵ, in the amplification, that is, $\tilde{A} = A \pm \epsilon$ we can say either $\tilde{A}_I = A_I \pm \delta_1$ or $\tilde{A}_S = A_S \pm \delta_2$. The area of the source star is determined by the source star radius, ρ, mass ratio, q, and the separation between the two lenses, s. Amplification as a function of time is dependent on the trajectory angle, α. The solution to this polynomial of 5th order contains either 3 or 5 images formed. To determine the total area of the 3 or 5 images, Green's theorem is used.[12] The magnification is given by the relative motion of the source star and lensing system.
In this work we examine single and binary lens caustics. A single lens event will have a caustic as a point. Hence the observed light curve should have a single peak as it approaches the caustic.

Binary lens caustics are more complicated and can be characterized by three different categories- Close, Intermediate, and Wide. The three categories are divided based on the combination of the mass ratio and the separation between the two lensing masses.[10] Binary sources as well as binary lenses could cause two peaks as depicted in our simulated light curves (Section 3). However, when generating light curves, we focus on the magnification due to binary lensing. Thus, a generalization of our CS results would be applicable for binary sources as well. Caustic curves represent closed loci where the magnification of a point source goes to infinity. Change in magnification as a function of time, depends on

1. ρ : source star radius
2. α: trajectory angle
3. q : ratio of the mass of the two lensing bodies
4. s: distance between the two lensing bodies

For a given q value, the topography changes to one, two, or three caustic curves based on the value of s. In terms of the magnification curve, the change in the number of caustics can result in different light curve signatures as the source crosses the caustic.

Mass ratio, q, and separation parameter, s, have a direct effect on the caustic topography generated. In this work, we focus on the error caused due to small changes, δ and ϵ, in q and s, respectively.

We show the error sensitivity for $\delta = 0.1q$ and $\epsilon = 0.1s$. In order to study error sensitivity, we choose points on the topography map in[11] well within each region, so that the change in the parameter does not result in a change in caustic topography.

For all our simulation analysis, we use sensitivity of 10%, hence $q \pm 0.1q$ and $s \pm 0.1s$.

2 Compressive Sensing Simulations Setup

Microlensing is typically detected in crowded stellar fields. Although the spatial images are densely populated, the microlensed events are very rare, hence, only stars with a transient magnification are of interest to astronomers. In order to eliminate constant star sources in crowded fields, differencing can be applied. Through our previous work,[13] we show that CS can be applied on crowded star fields to produce differenced images, preserving the microlensed star magnification, with very low error when the point spread function (PSF) of the two differenced images are the same.

2.1 Compressive Sensing Architecture and Process

In our simulations, we use CS framework based on our previous work.[13] An architectural diagram is shown in Figure 3.

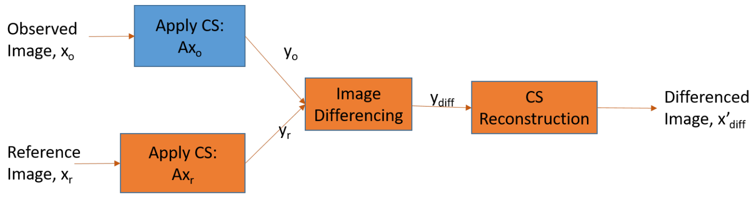

Fig 3: CS Architecture used for obtaining differenced images with star sources varying in flux due to a gravitational microlensing event

In this work, we define a reference image, x_r, as an image of a spatial region, x, with a PSF, P_r, while an observed image, x_o, is defined as an image of the same spatial region, x, but with a different PSF, P_o. A reference image has a narrower PSF, resulting in a cleaner image as compared to an observed image. The architecture is implemented in the following manner:

1. Obtain CS based measurements, y_o, for a spatial image.
   CS can be applied by projecting a matrix, A, onto the region of interest, x_o. This can be done on a column-by-column basis for a n x n spatial region, x_o. Thus, for 2D images, y_0 and A are of size m x n, where $m << n$.

2. Given A and a clean reference image, x_r, construct measurements matrix y_r, where $y_r = Ax_r$.

3. Apply a 2D differencing algorithm on y_o and y_r to obtain a differenced image, y_{diff}, and the corresponding convolution kernel, M, which is used to match the observed and reference CS measurement vectors, y_o and y_r.[14] In our modelling, we use $y_{diff} = y_o - y_r$, by using the assumption that the PSF of the reference and observed image is the same as discussed in Section 2.2.

4. Reconstruct the differenced image, x'_{diff} using CS reconstruction algorithms, given A and y_{diff}.

2.2 *Assumptions in our Model*

To understand merely the effects of Compressive Sensing on photometric measurements, we eliminate the following variables in our simulations. In future work, we will incorporate each of these factors in one at a time to thoroughly understand the effect of each one in our CS based framework. The two assumptions we make are:

1.) The PSF of the reference image and the observed image is the same. This would typically be the case for space-borne observatories in which the PSF changes very slowly, if at all. The two images differ in any magnification of a star source due to a transient event.
In applications where the PSF of the reference and observed images are different, equation 16 is used.

$$y_{diff} = Ax_o - (Ax_r \star M) \tag{15}$$
$$= y_o - (y_r \star M) \tag{16}$$

However, in our models, for simplicity, we assume the same PSF for a reference and observed image, thus resulting in equation 19.

$$
\begin{aligned}
y_{diff} &= A(x_{diff}) && (17)\\
&= A(x_o) - A(x_r) && (18)\\
&= y_o - y_r && (19)
\end{aligned}
$$

Hence, in Figure 3, image differencing consists of subtracting the reference measurements from the observed measurements. In non-ideal cases, when the PSF of the reference image is different as compared to the observed image, image differencing algorithms can be added. However, that adds another layer of uncertainty and error, which we needed to eliminate for our purpose of understanding purely the effects of compressive sensing acquisition and reconstruction.

2.) There is no noise present.
To eliminate added complexity in this preliminary study, we do not incorporate any noise. In future studies, we will add in detector noise, measurement noise, as well as any background noise.

For a practical approach, we can assume the effects of noise to be minimal if the SNR during a magnification event for the specific group of pixels representing the microlensing star is sufficiently high, such that, the sparsity content of the image is preserved. In section 3, we briefly show the basic effect of CS reconstruction for degrading SNR for an image with Gaussian added noise.

2.3 Simulation Setup Parameters

In our simulations, we use a 128 x 128 size image. In order to depict a crowded stellar field, we generate the number of star sources to be 75% of the total number of pixels. To simulate realistic fields, we use Airy shaped PSFs with varying radius and flux of the star sources. The radius ranges from $[0, 5]$ pixel units and flux ranges from $[50, 5000]$ pixel counts. We perform 100 Monte Carlo simulations for each set of parameter values discussed later in this section. For each of the 100 Monte Carlo simulations, the crowded stellar field is changed, including the PSF radius and flux values of each star source generated. In addition, for each of the simulation, the Bernoulli random values in A are changed. We use Orthogonal Matching Pursuit algorithm, as provided by Python libraries, for reconstruction.

Compressive Sensing Parameters

For a n x n size spatial image, we use a measurement matrix, A, of size m x n to obtain the measurements, y, of size m x n. Hence, our compression factor is $\frac{m}{n}$.
For both single lens and binary lens event simulations, we use the following CS parameters.

- Number of measurements, $m = 25\%$ of n
- Measurement matrix, A, consists of Bernoulli random variables of values 1 and 0. These values were chosen such that the matrix can be relevant for practical application.

Gravitational Microlensing Parameters

We simulate microlensing events for single lens and binary lens systems.

I Single Microlensing events

For single lens systems we use the following parameters and for each of the simulation cases, u_0 and t_0 are varied in the simulation setup.The other parameters from equation 6 are shown in Table 1.

Parameter	Value
u_0	0.01, 0.1, 0.5
t_0	13, 15, 17
t_e	30

Table 1: Single microlensing event equation parameters used for CS simulation modelling

II Binary Microlensing events

For binary microlensing events, we perform simulations for each of the three topographies with the parameter list shown below.

Parameter	Close	Intermediate	Wide
s	0.6	1	1.7
q	1	0.1	0.01
ρ	0.01	0.01	0.01
α	0.03	0.93	0.03
t_E	100.3	100.3	100.3
t_0	7154	7154	7154
u_0	0.1	0.2	0.3

Table 2: Binary microlensing event equation parameters used for CS simulation modelling

The description of parameters show in Table 2 is given below:

1) s: separation between the two masses in the lensing system in units of total angular Einstein radii

2) q: Mass ratio of the two lenses

3) ρ: Source radius in units of Einstein's ring raidus

4) α Trajectory angle between lens axis and source

5) t_E: Einstein ring radius crossing time

6) t_0: Time of peak magnification

7) u_0: Impact parameter in units of Einstein's ring radius

Error Calculations

We calculate % error based on total flux of the microlensing star in a 3 pixel unit radius from the center pixel of the star. Error is calculated using

$$\frac{|f'_{diff} - f_{diff}|}{f_{diff}} \times 100\% \quad (20)$$

where f'_{diff} and f_{diff} are the total fluxes within the 3-pixel radius of the source positions of the reconstructed and original differenced images, respectively.

3 Simulation Results

3.1 Single Lens Events

In these first set of simulations, we vary u_0, while keeping $t_0 = 15$ and $t_e = 30$ constant. Amplification for single lens microlensing events are generated using equation 6. We compare the CS reconstruction with error due to a γ change in θ_E as described in equation 11, where $\gamma = 1 \pm 0.1$. Hence $\theta_E = 0.9\theta_E$ and $\theta_E = 1.1\theta_E$.

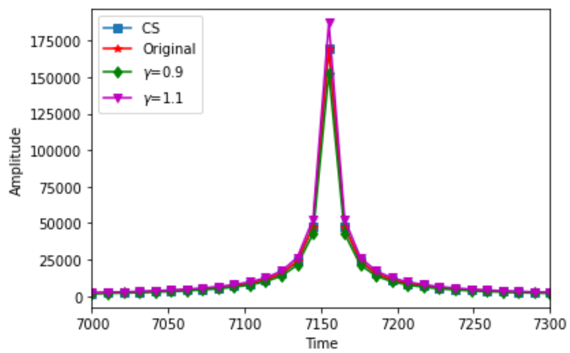

Fig 4: Single Lens microlensing event, $u_0 = 0.01$.
The original simulated microlensing curve along with the CS reconstruction, and the microlensing curve generated due to a change γ in θ_E is shown

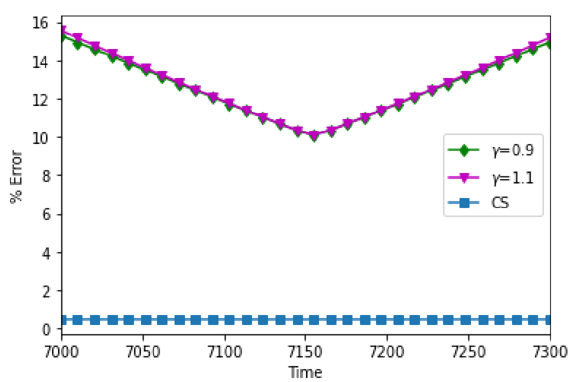

Fig 5: % Errors for Single Lens event, $u_0 = 0.01$ for CS reconstruction and the change in microlensing light curve generated due to γ changes in θ_E as compared to the original simulated microlensing curve for the light curves in Figure 4

Single lens event with $u_0 = 0.01$	Average % error	Average standard deviation
CS	0.49	0.00
γ = 0.9	12.62	1.53
γ = 1.1	12.71	1.61

Table 3: Errors for single microlensing light curve with $u_0 = 0.01$

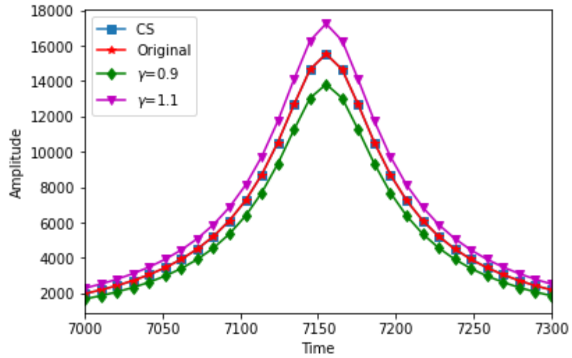

Fig 6: Single Lens microlensing event, $u_0 = 0.1$.
The original simulated microlensing curve along with the CS reconstruction, and the microlensing curve generated due to a change in γ in θ_E is shown

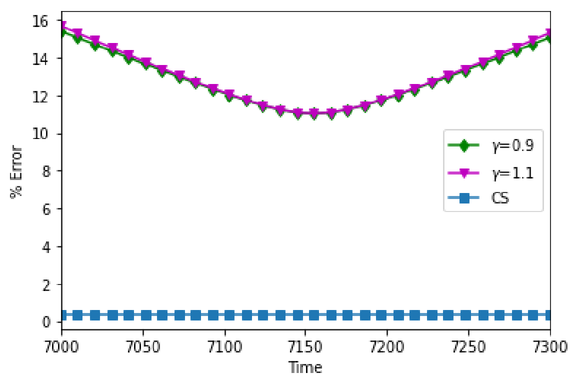

Fig 7: % Errors for Single Lens event, $u_0 = 0.1$ for CS reconstruction and the change in microlensing light curve generated due to γ changes in θ_E as compared to the original simulated microlensing curve for the light curves in Figure 6

Single lens event with $u_0 = 0.1$	Average % error	Average standard deviation
CS	0.36	0.00
$\gamma = 0.9$	12.91	1.36
$\gamma = 1.1$	13.01	1.43

Table 4: Errors for single microlensing light curve with $u_0 = 0.1$

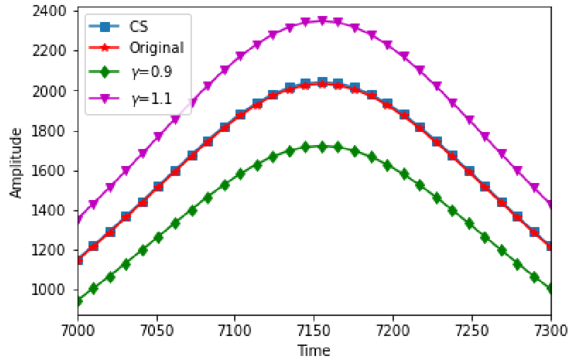

Fig 8: Single Lens microlensing event, $u_0 = 0.5$.
The original simulated microlensing curve along with the CS reconstruction, and the microlensing curve generated due to a change in γ in θ_E is shown

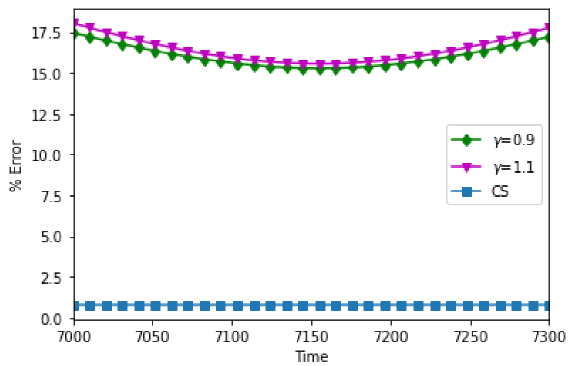

Fig 9: % Errors for Single Lens event, $u_0 = 0.5$ for CS reconstruction and the change in microlensing light curve generated due to γ changes in θ_E as compared to the original simulated microlensing curve for the light curves in Figure 8

Single lens event with $u_0 = 0.5$	Average % error	Average standard deviation
CS	0.77	0.00
$\gamma = 0.9$	16.07	0.66
$\gamma = 1.1$	16.45	0.76

Table 5: Errors for single microlensing light curve with $u_0 = 0.5$

229 In the next set of simulations, we use $u_0 = 0.1$ and vary t_0 with $t_0 = 13$ and $t_0 = 17$.

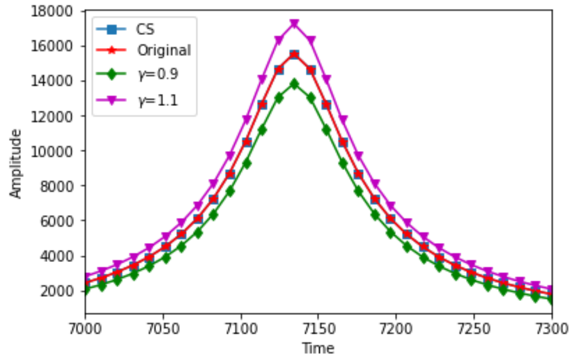

Fig 10: Single Lens microlensing event, $t_0 = 13$.
The original simulated microlensing curve along with the CS reconstruction, and the microlensing curve generated due to a change in γ in θ_E is shown

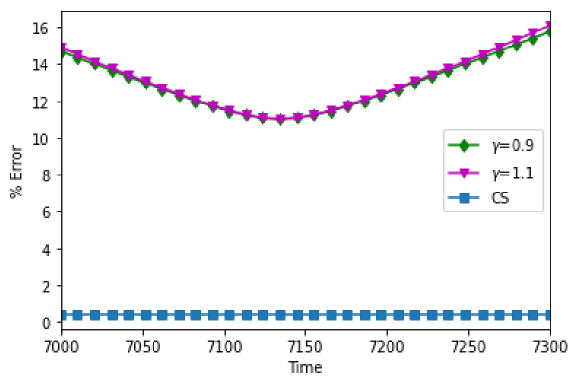

Fig 11: % Errors for Single Lens event, $t_0 = 13$ for CS reconstruction and the change in microlensing light curve generated due to γ changes in θ_E as compared to the original simulated microlensing curve for the light curves in Figure 10

Single lens event with $t_0 = 13$	Average % error	Average standard deviation
CS	0.42	0.00
γ = 0.9	12.94	1.40
γ = 1.1	13.03	1.48

Table 6: Errors for single microlensing light curve with $t_0 = 13$

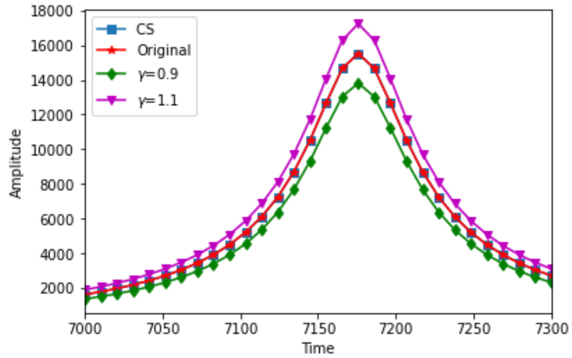

Fig 12: Single Lens microlensing event, $t_0 = 17$.
The original simulated microlensing curve along with the CS reconstruction, and the microlensing curve generated due to a change in γ in θ_E is shown

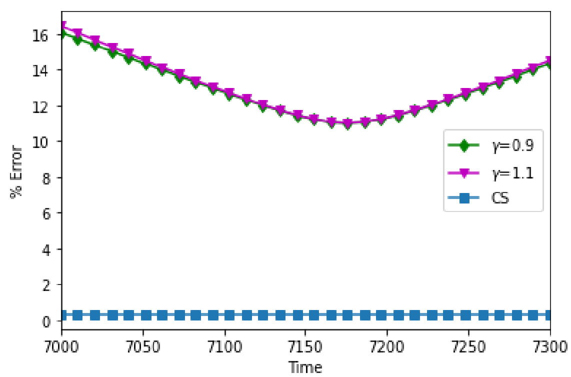

Fig 13: % Errors for Single Lens event, $t_0 = 17$ for CS reconstruction and the change in microlensing light curve generated due to γ changes in θ_E as compared to the original simulated microlensing curve for the light curves in Figure 12

Single lens event with $t_0 = 17$	Average % error	Average standard deviation
CS	0.32	0.00
γ = 0.9	12.98	1.48
γ = 1.1	13.09	1.57

Table 7: Errors for single microlensing light curve with $t_0 = 17$

Our simulations show that CS reconstruction is affected by the magnification value of the source star in each differenced image. For low magnification events, such as the one caused by $u_0 = 0.5$, the error in CS reconstruction is higher. The results in[13] also indicate that CS reconstruction accuracy is dependent on the magnification of the event, which in turn affects the sparsity of the data set. For low magnification star in a differenced image, the rate of decay of the coefficients in the differenced images also decreases, hence, causing a higher error in CS reconstruction. The small fluctuations in the average error are due to the variation in Bernoulli random measurement matrix. From the error plots (7, 9, 5), we see that CS error is fairly constant, with little variability, over the microlensing curves for all u_0 and t_0 values.

3.1.1 Noise effects on a Single Lens Microlensing Event Curve

In this section, we briefly show the effect of Gaussian noise on the reconstruction of the microlensing event curves. From CS theory, it is known that the signal of interest is accurately reconstructed for sparse signals. Hence, adding noise to the spatial images can degrade the sparsity of the images. In our simulations, we add random Gaussian noise with mean = 0, and varying standard deviation to obtain images with different SNRs. CS architecture shown in Figure 3 is applied, with the noise application on the observed image, x_o. In the noise simulation, 25% CS measurements were used.

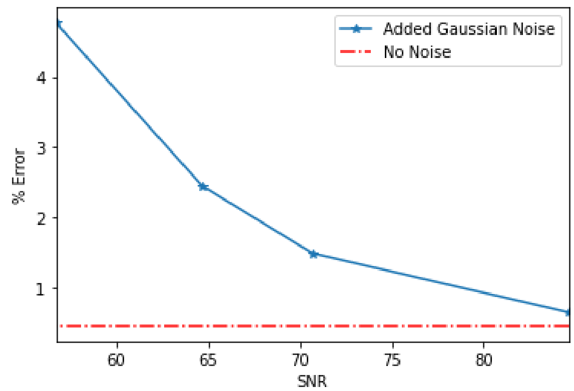

Fig 14: $\%$ error as a function of image SNR. Images are generated by varying added Gaussian noise. The dashed red line represents $\%$ error without any addition of noise

From Figure 14, it is evident that as the SNR decreases, the $\%$ of error increases at a higher rate. The rate of increase is 0.06 % error per SNR unit towards the higher SNR values and 0.29 % error per SNR unit towards the lower SNR range.

3.2 Binary Lens Microlensing Events

The amplification for the photometric curves is derived using gravitational microlensing equations, generated by the software provided in.[12]

We perform simulations on the three categories described in Section 1.4 - close, intermediate, and wide. To determine error sensitivity in terms of impact on the separation parameter, s, and mass ratio, q, we compare the CS reconstruction with the following values of s and q, thereby providing CS reconstruction accuracy bounds of 10% for the value of s and q.

Caustic	Original s	$\pm 0.1s$	Original q	$\pm 0.1q$
Close	0.6	0.54, 0.66	1	0.9, 1.1
Intermediate	1	0.9, 1.1	0.1	0.09, 0.11
Wide	1.7	1.53, 1.87	0.01	0.009, 0.011

Table 8: Values of s and q chosen for calculating error sensitivity, such that it is within 10% of the value chosen for the original caustic

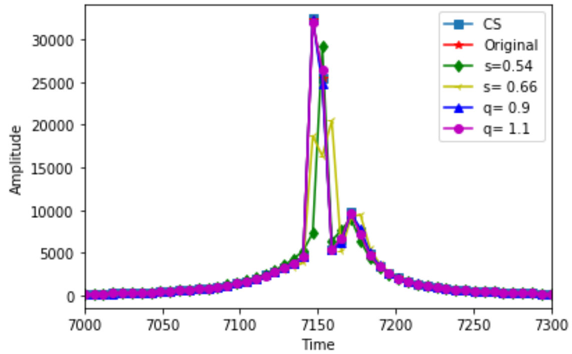

Fig 15: Closed caustic microlensing curve with s = 0.6 and q = 1, shown along with the CS reconstruction, as well as the microlensing curve generated using s= 0.54, 0.66 and q = 0.9, 1.1

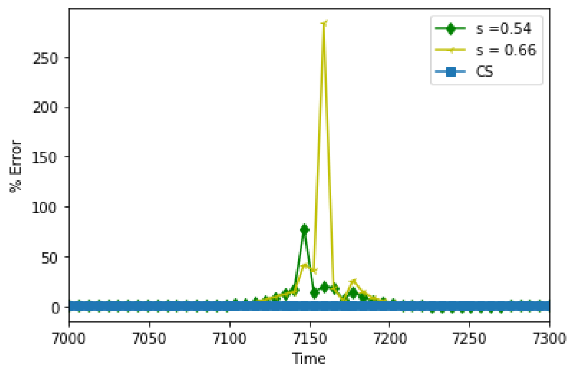

Fig 16: $\%$ error of CS reconstruction as compared to $\%$ error due to 10% deviation in the value of s.

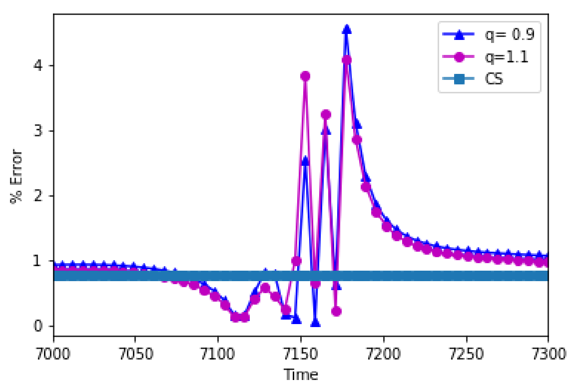

Fig 17: $\%$ error of CS reconstruction as compared to $\%$ error due to 10% deviation in the value of q

$Close Caustic$	Average % Error	Avg Standard deviation of the % error
CS	0.76	0.00
s= 0.54	0.52	11.52
s= 0.66	10.47	40.02
q= 0.9	1.11	0.80
q= 1.1	1.07	0.82

Table 9: Errors for close caustic topographies model for CS reconstruction, and for microlensing light curve generated due to 10% variation in s and q

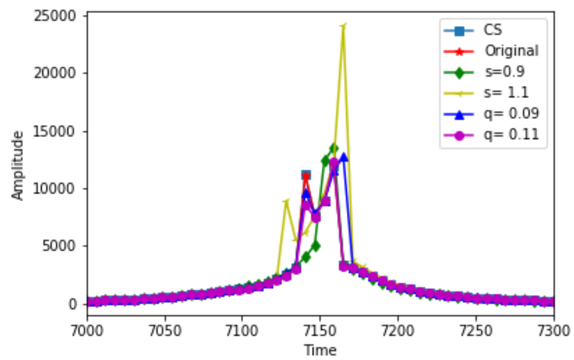

Fig 18: Intermediate caustic microlensing curve with s = 1 and q = 0.1, shown along with the CS reconstruction, as well as the microlensing curve generated using s= 0.9, 1.1 and q = 0.09, 0.11

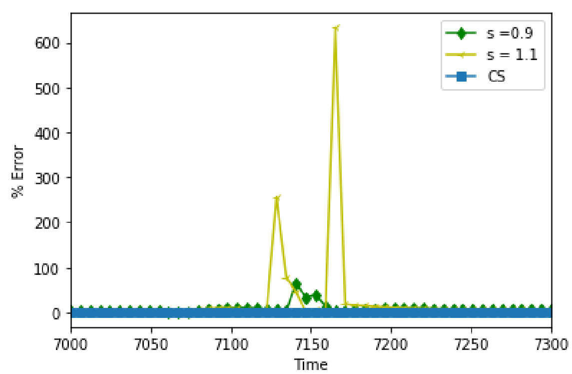

Fig 19: $\%$ error of CS reconstruction as compared to $\%$ error due to 10% deviation in the value of s for the given (Figure 18) intermediate caustic binary lensing light curve reconstruction

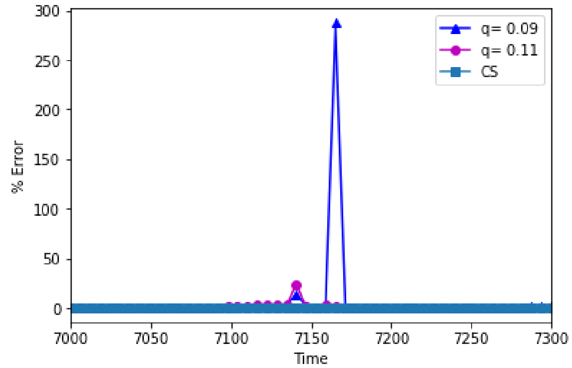

Fig 20: % error of CS reconstruction as compared to % error due to 10% deviation in the value of q for the given (Figure 18) intermediate caustic binary lensing light curve reconstruction

Intermediate Caustic	Average % Error	Avg Standard deviation of the % error
CS	0.61	0.00
s= 0.9	7.74	10.45
s= 1.1	25.86	94.24
q= 0.09	6.76	40.14
q= 0.11	1.13	3.23

Table 10: Errors for intermediate caustic topographies model for CS reconstruction, and for microlensing light curve generated due to 10% variation in s and q

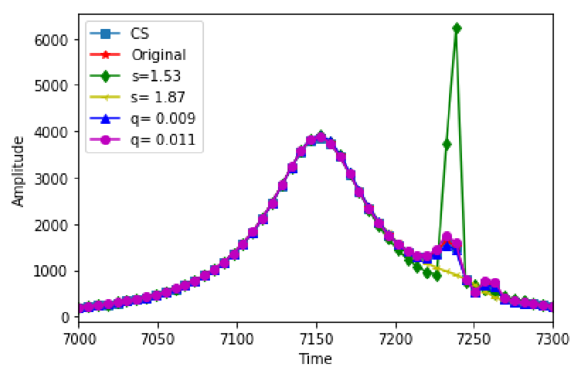

Fig 21: Wide caustic microlensing curve with s = 1.7 and q = 0.01, shown along with the CS reconstruction, as well as the microlensing curve generated using s= 1.53, 1.87 and q = 0.009, 0.011

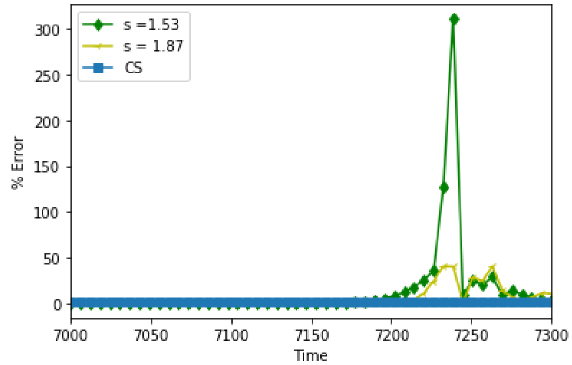

Fig 22: $\%$ error of CS reconstruction as compared to $\%$ error due to 10% deviation in the value of s for the given (Figure 21) wide caustic binary lensing light curve reconstruction

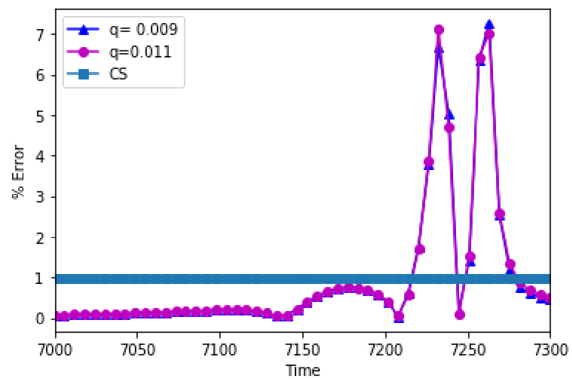

Fig 23: $\%$ error of CS reconstruction as compared to $\%$ error due to 10% deviation in the value of q for the given (Figure 21) wide caustic binary lensing light curve reconstruction

Wide Caustic	Average $\%$ Error	Avg Standard deviation of the $\%$ error
CS	0.97	0.00
s= 1.53	13.64	46.57
s= 1.87	5.54	11.02
q= 0.009	0.96	1.73
q= 0.011	0.97	1.74

Table 11: Errors for wide caustic topographies model for CS reconstruction, and for microlensing light curve generated due to 10% variation in s and q

Our simulations show that we can attain error less than 1% using 25% of the Nyquist rate measurements. In addition, the error obtained through CS reconstruction, will be well within 10% deviation in verified microlensing parameters of θ_E, s and q.

4 Conclusions and Future Work

Using this technique we give limitations on the sensitivity of detection of planetary perturbations given our CS parameters. We show examples of the effects of error tolerance on the science parameters that are of importance in the microlensing curves. For both single and binary microlensed events, we provide examples of the changes in the microlensing parameters due to minimal error tolerance. This gives a bound for analyzing the effects of compressive sensing for the application of gravitational microlensing. These are simulated theoretical error bounds for given sensitivities- the sensitivity of the detectors and technology currently used may not be sensitive to such δ changes in the science parameters. For single lensed microlesning events, we showed the CS reconstruction error as compared to error from $\pm$ 10% in θ_E. Our results show that CS is sensitive to changes in u_0 and not to changes in t_0, as t_0 causes merely a shift in data, while u_0 causes a change in magnification value. For binary lensed microlensing events, we show CS reconstruction error as compared to error within $\pm$ 10% of the mass ratio and the separation between the two lenses. Our work shows that we can reconstruct microlensing light curves using 25% of the required Nyquist rate measurements with error less than 1%. In terms of microlensing sensitivity, we show that this error is within the bounds of 10% of θ_E for single microlensed events and within 10% of q and s for binary microlensed events. In this work we only focus on bounds determined by our simulated models using microlensing theory and disregard detector optics effects. In cases where less sensitivity is affordable, fewer measurements can be used to further save on-board resources. Vice Versa, if more sensitivity to perturbations is required the number of measurements can be increased. This technique works with high accuracy, with less than 1% error for crowded stellar fields with the same PSFs for a reference and observed image.

Our future work will incorporate noise analysis, as well as the implementation of this CS architecture for reference and observed images with different PSFs. In the case of different PSFs, we will understand the efficacy of differencing algorithms used in astronomical applications.

4.1 Disclosures

There are no conflicts of interest

References

1 Korde-Patel, Asmita, Richard K. Barry, and Tinoosh Mohsenin."Application of Compressive Sensing to Gravitational Microlensing Experiments." Proceedings of the International Astronomical Union 12.S325 (2016): 67-70.

2 Korde-Patel, Asmita, Richard K. Barry, and Tinoosh Mohsenin. "Application of Compressive Sensing to Gravitational Microlensing Data and Implications for Miniaturized Space Observatories." (2016).

3 Starck, Jean-Luc, Fionn Murtagh, and Jalal M. Fadili. Sparse image and signal processing: wavelets, curvelets, morphological diversity. Cambridge university press, 2010.

4 Rebollo-Neira, Laura, and James Bowley. "Sparse representation of astronomical images." JOSA A 30.4 (2013): 758-768.

5 Eldar, Yonina C., and Gitta Kutyniok, eds. Compressed sensing: theory and applications. Cambridge university press, 2012.

6 Candès, Emmanuel J., and Michael B. Wakin. "An introduction to compressive sampling [a sensing/sampling paradigm that goes against the common knowledge in data acquisition]." IEEE signal processing magazine 25.2 (2008): 21-30.

7 Candes, Emmanuel, and Justin Romberg."Sparsity and incoherence in compressive sampling." Inverse problems 23.3 (2007): 969.

8 Wakin, Michael B., et al.“An architecture for compressive imaging.” 2006 International Conference on Image Processing. IEEE, 2006.

9 Pope, Graeme. Compressive sensing: A summary of reconstruction algorithms. MS thesis. ETH, Swiss Federal Institute of Technology Zurich, Department of Computer Science, 2009.

10 Seager, Sara.“Exoplanets.” Exoplanets (2010).

11 Tsapras, Yiannis. ”Microlensing searches for exoplanets.” Geosciences 8.10 (2018): 365.

12 V. Bozza, Microlensing with an advanced contour integration algorithm: Green’s theorem to third order, error control, optimal sampling and limb darkening, Monthly Notices of the Royal Astronomical Society, Volume 408, Issue 4, November 2010, Pages 2188–2200, https://doi.org/10.1111/j.1365-2966.2010.17265.x

13 Korde-Patel, Asmita, Richard K. Barry, and Tinoosh Mohsenin. ”Compressive Sensing Based Data Acquisition Architecture for Transient Stellar Events in Crowded Star Fields.” 2020 IEEE International Instrumentation and Measurement Technology Conference (I2MTC). IEEE, 2020.

14 Bramich, D. M.“A new algorithm for difference image analysis.” Monthly Notices of the Royal Astronomical Society: Letters 386.1 (2008): L77-L81.

5 Author Biographies

Asmita Korde-Patel is a civil servant at NASA Goddard Space Flight Center in the Instrument Electronics Development branch. She works on implementing algorithms onto hardware for space flight instruments. She is currently pursuing her PhD in electrical engineering at University of Maryland, Baltimore County. Her research interest lies in applying compressive sensing (CS) to transient photometric measurements. Specifically, she is studying the effects of CS application for gravitational microlensing, a technique used to detect exoplanets.

Richard K. Barry is an astronomer in NASA’s Laboratory for Exoplanets and Stellar Astrophysics. His principal research involves the detection and characterization of new exoplanets using the techniques of gravitational microlensing and transits. Previously, Dr. Barry has worked as a NASA Space Shuttle Engineer, power systems engineer, instrument design engineer and USAF technician on F16 aircraft.

Tinoosh Mohsenin is an Associate Professor with the Department of Computer Science and Electrical Engineering at University of Maryland, Baltimore County. She received her PhD from University of California, Davis in 2010. She has authored or co-authored over 130 peer-reviewed journal and conference publications. Her research focus is on designing energy efficient embedded processors for machine learning and signal processing, knowledge extraction techniques for autonomous systems, wearable smart health monitoring, and embedded big data computing.

List of Figures